Three Synthetic Routes to Single-Crystalline PbS Nanowires with Controlled Growth Direction and Their Electrical Transport Properties

So Young Jang,[†] Yun Mi Song,[†] Han Sung Kim,[†] Yong Jae Cho,[†] Young Suk Seo,[†] Gyeong Bok Jung,[†] Chi-Woo Lee,[†] Jeunghee Park,[†,*] Minkyung Jung,[‡] Jinhee Kim,[‡] Bongsoo Kim,[§] Jin-Gyu Kim,[⊥] and Youn-Joong Kim[⊥]

[†]Department of Chemistry, Korea University, Jochiwon 339-700, Korea, [‡]Korea Research Institute of Standards and Science, Daejeon 305-600, Korea, [§]Department of Chemistry, KAIST, Daejeon 305-701, Korea, and [⊥]Division of Electron Microscopic Research, Korea Basic Science Institute, Daejon 305-333, Korea

ABSTRACT Single-crystalline rock-salt PbS nanowires (NWs) were synthesized using three different routes; the solvothermal, chemical vapor transport, and gas-phase substitution reaction of pregrown CdS NWs. They were uniformly grown with the [100] or [110], [112] direction in a controlled manner. In the solvothermal growth, the oriented attachment of the octylamine (OA) ligands enables the NWs to be produced with a controlled morphology and growth direction. As the concentration of OA increases, the growth direction evolves from the [100] to the higher surface-energy [110] and [112] directions under the more thermodynamically controlled growth conditions. In the synthesis involving chemical vapor transport and the substitution reaction, the use of a lower growth temperature causes the higher surface-energy growth direction to change from [100] to [110]. The high-resolution X-ray diffraction pattern and X-ray photoelectron spectroscopy results revealed that a thinner oxide-layer was produced on the surface of the PbS NWs by the substitution reaction. We fabricated field effect transistors using single PbS NW, which showed intrinsic *p*-type semiconductor characteristics for all three routes. For the PbS NW with a thinner oxide layer, the carrier mobility was measured to be as high as 10 $cm^2 V^{-1} s^{-1}$.

KEYWORDS: PbS nanowires · controlled growth direction · solvothermal · chemical vapor transport · gas-phase substitution · field effect transistors

Since the discovery of carbon nanotubes (CNTs), a tremendous amount of research has been conducted on the synthesis and utilization of one-dimensional (1D) nanostructures (nanorods, nanowires, nanobelts, *etc.*) as well-defined building blocks for future nanodevices using "bottom up" approaches.[1,2] The success of various applications such as high-performance optoelectronic devices, field-effect transistors, logic circuits, nonvolatile memories, and biosensors depends on the quality control of the nanostructures.[3−5] The development of cost-effective techniques for the synthesis of high-quality 1D nanostructures with the desired properties is an important milestone on the way toward their broad commercial application.

As one of the important IV−VI semiconductor materials, rock-salt (face-centered cubic) structured lead sulfide (PbS) nanostructures have been the object of particular attention, because of the narrow band gap (0.41 eV in the bulk form at room temperature) and strong quantum confinement effect owing to its large Bohr radius (*ca.* r_B = 18 nm).[6] PbS nanostructures exhibit a wide range of potential applications, such as IR emission and detection, biological imaging, photovoltaics, and solar cells.[7−11] In particular, there have been a number of reports on the successful synthesis of PbS NWs using various methods, including the template-assisted deposition,[12−14] hydrotherthermal,[15−20] solvothermal,[21−28] chemical vapor transport (CVT),[29−34] pyrolysis,[35] and electron-beam irradiation techniques.[36] However, developing an improved synthesis method that increases the yield of PbS NWs with a controlled morphology and crystal structure still remains quite a challenge.

To enable anisotropic 1D crystal growth, the oriented attachment of a protecting ligand has been employed as an important strategy in solvothermal synthesis. CVT synthesis utilizes the well-known vapor−liquid−solid (VLS) growthmechanism, in which catalytic metal nanoparticles form low-melting point eutectic alloys with the target materials to serve as seeds. In previous studies, both synthesis methods produced exclusively rock-salt PbS NWs with the [100] growth direction.[21−34] Among the other versatile growth methods, the substitution technique (so-called chemical conversion or chemical templating) has been

*Address correspondence to parkjh@korea.ac.kr.

Received for review January 27, 2010 and accepted March 18, 2010.

Published online March 29, 2010. 10.1021/nn100163k

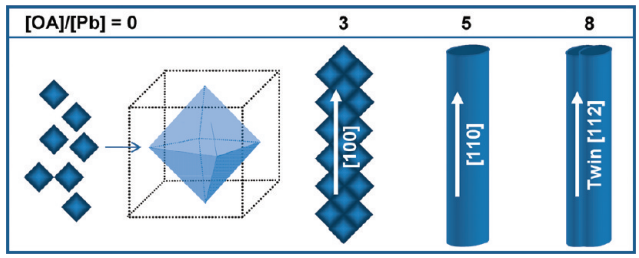

Scheme 1. Evolution of the morphology and growth direction of the PbS NWs by increasing the concentration of OA.

successfully used to synthesize 1D nanostructures.[37−56] Alivisatos group reported the solution-phase synthesis of PbS nanorods, using cation exchange reaction of CdS nanorods, through the CdS−Cu_2S heterostructure form.[47] Nevertheless, no gas-phase substitution reaction has been developed for the synthesis of PbS NWs so far. To the best of our knowledge, moreover, there have been no comparative and systematic studies on the controlled morphology and growth direction of PbS NWs for these three different synthesis methods.

In the present work, we report single-crystalline PbS NWs synthesized using three methods: (i) the solvothermal reaction, (ii) CVT, and (iii) gas-phase conversion reaction of pregrown CdS NWs as templates. In the solvothermal growth, octylamine was used as a ligand offering "sufficient" protection, which causes the progressive evolution of the morphology and growth direction of the PbS NWs. The CVT method using $PbCl_2$ and sulfur (S) as the precursors under argon flow enables single-crystalline PbS NWs to be grown. The gas-phase conversion of the CdS NWs into PbS NWs involves the substitution reaction, which alters the cation composition without changing the original outward appearance of the NWs. For both the CVT and substitution methods, we demonstrated that the growth direction is controllable, mainly by adjusting the growth temperature. Remarkably, for the first time, the growth direction of the PbS NWs was commonly controlled between [110], [100], and [112] by the growth strategy of each method. High-resolution X-ray diffraction and X-ray photoelectron spectroscopy were employed to examine the surface structure of the NWs, which can depend on the growth method. We also fabricated field-effect transistors (FET) using single PbS NW, showing them to be intrinsically *p*-type semiconductors, for all these NWs. The highest carrier mobility was obtained from the highest-quality PbS NWs synthesized by the substitution reaction.

RESULTS AND DISCUSSION

Morphology Controlled Solvothermal Synthesis of PbS NWs Using Octylamine Ligand. The evolution of the morphology and growth direction of the PbS NWs by increasing the concentration of OA was summarized in Scheme 1. Figure 1a displays the TEM image of the PbS nanocrystals (NCs) synthesized at 270 °C for 10 min without OA. The shape of the NCs is octahedral and their average diameter is about 20 nm. The HRTEM image and fast Fourier-transform (FFT) ED pattern (zone axis = [111]) generated from the inversion of the TEM image using Digital Micrograph GMS1.4 software (Gatan Inc.), as shown in the insets, confirm the single-crystalline octahedral NCs having the lateral [110] direction. As the OA is added at a ratio of PbO:OA = 1:1, the zigzagged-shaped NWs start to be produced, as shown in Figure 1b. As the concentration of OA increases to a ratio of PbO:OA = 1:3, the PbS NWs are exclusively synthesized (Figure 1c). The diameter of the NWs is in the range of 40−60 nm with an average value of 50 nm. Figure 1d corresponds to their SEM image, showing their high yield and uniformity. Figure 1e shows the high-resolution TEM (HRTEM) images of a selected zigzagged NW, revealing its perfect single-crystalline nature. The (200) fringes are separated by a distance of 3.0 Å, which is equal to that of cubic bulk PbS crystal (a = 5.931 Å; JCPDS card no. 78-1058). The corresponding selected-area ED (SAED) pattern, measured at the [011] zone axis, confirms the [100] growth direction (inset). The facet of the zigzagged surface is matched to the {111} planes of the cubic unit cell. The EDX analysis confirms that the NWs were composed of Pb and S at a ratio of 1 ± 0.1, as shown in the Supporting Information, Figure S1. We refer to the PbS NWs synthesized using PbO:OA = 1:3 as "**PS1**".

As the concentration of OA increases to a ratio of PbO:OA = 1:5, the shape of the NWs becomes straight, and the average diameter of the NWs decreases to 30 ± 5 nm (Figure 1f). Under these conditions, the yield of these straight NWs is much lower than that of the zigzagged ones. Figure 1g shows the HRTEM images and corresponding SAED pattern (zone axis = [111]), confirming their [110] growth direction (inset). The (220) fringes are separated by a distance of 2.1 Å, which is equal to that of cubic PbS crystal. As the concentration of OA increases to a ratio of PbO:OA = 1:8, thicker NWs (average diameter = 50 ± 10 nm) are formed (Figure 1h). A close look reveals that these NWs consisted of two segments (average diameter = 20−30 nm) jointed along the axial direction. Figure 1i and the inset show the HRTEM images of a representative bicrystalline NW and the corresponding FFT ED pattern (zone axis = [011]). This PbS NW has the [112] growth direction with a twinned structure in which the two NW segments share the $[111]_c$ and $[\bar{1}\bar{1}\bar{1}]_c$ spots, which is perpendicular to the growth direction. (i) and (iii) correspond to the ED patterns of the individual NW segment and (ii) corresponds to that of the twin plane region. The (111) fringes are separated by a distance of 3.4 Å, which is equal to that of cubic bulk PbS crystal.

A number of works reported that amine capping ligands play an important role in inducing the 1D growth of many metals and semiconductors NC, in addition to stabilizing the NCs.[57−79] It is anticipated that

with its higher nucleophilic nature, OA would be bound to the positive ions of the growing nanocrystals, similarly to the other amines (i.e., oleylamine, trioctylamine, hexadecylamine, *etc.*) that were used in previous works. The inherent anisotropy of the surface energies associated with the surface reactivity and/or dipolar interactions was suggested to be the driving force for the 1D growth.[80,81] In the cubic unit cell system, there is a general sequence in the surface energy of the crystallographic planes; {111} < {100} < {110}.[82] The growth along the higher surface-energy planes could have the lower activation energy barrier. The controlled morphology and growth direction of the PbS NWs obtained by varying the concentration of OA is thought to be strongly related to the relative surface energy of these planes.

Without OA, the reaction product is octahedral NCs terminated by eight {111} facets (see Scheme 1). As the OA is added to the reaction mixture as a cosurfactant, the NWs start to grow with a zigzagged morphology that originates from the assembly of the octahedral NC building blocks. The NCs are driven to attach to the higher surface energy planes {100} of the growing NWs. Since the nucleophilic OA binds strongly to the crystal surface, the growth rate would decrease, thus allowing more time for the diffusion of the atoms on the crystal surface. Therefore, the growth is expected to occur under thermodynamically controlled conditions, and such an incubation-like process induces the preferred attachment along the [100] direction, which has a higher surface energy than the [111] direction.

As the OA concentration increases further to PbO:OA = 1:5, the chainlike assemblies evolve to straight NWs with a narrower diameter. These PbS NW are uniformly grown along the [110] direction. In the presence of excess OA, the nucleation of the PbS seeds would be further delayed. The existence of this longer induction period between the injection of the stock solution and nucleation of the nanocrystals allows for the good intermixing of the reactants and thermal equilibration of the reaction mixture. Then, the NW growth would occur more slowly through the higher surface-energy [110] direction than the [100] direction. This, in turn, improves the surface evenness and narrows the diameter distribution.

As the OA concentration increases to PbO:OA = 1:8, the NWs evolve from a straight to twinned morphology with the [112] growth direction. The higher concentration of OA decreases the growth rate further, allowing growth to take place along the much higher surface-energy direction associated with the higher index planes, that is {112}. The twinning process leads to a defect structure in which two subgrains share a common crystallographic plane; that is, the structure of one subgrain is the mirror reflection of the other in the

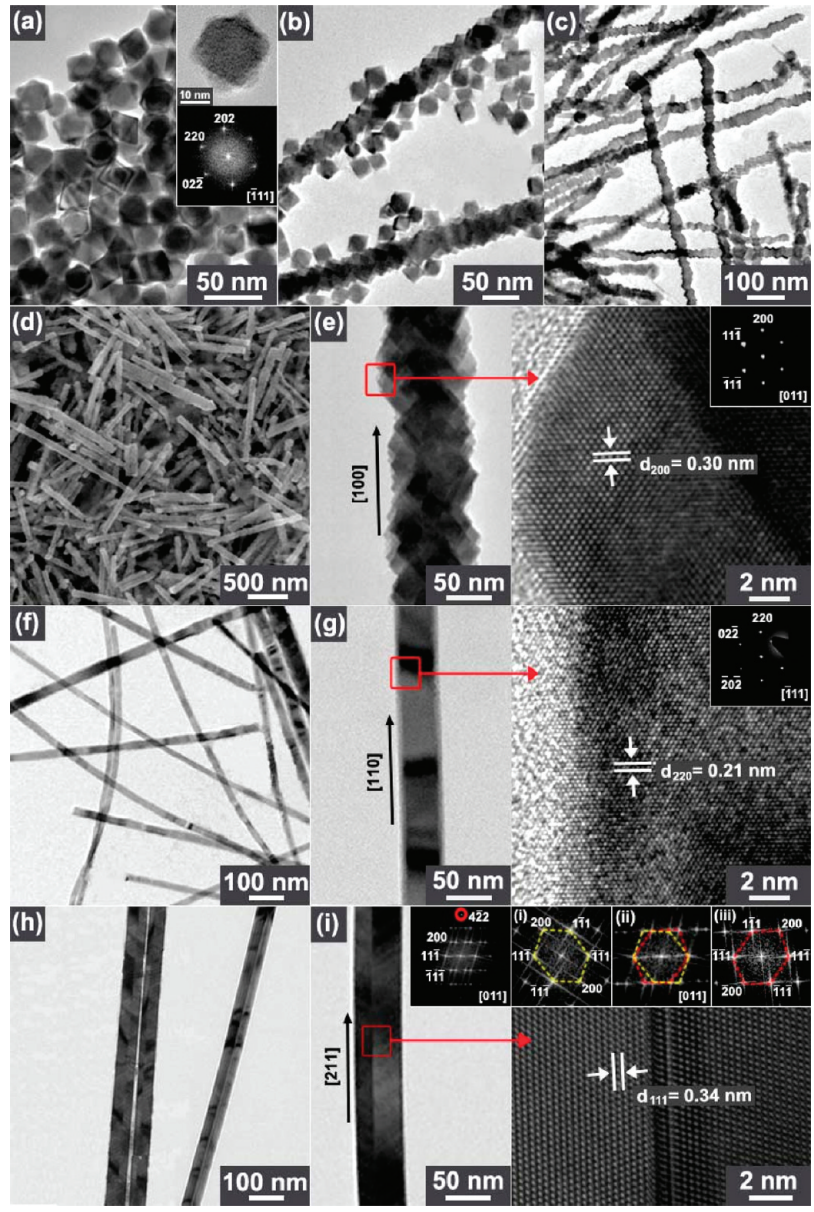

Figure 1. (a) TEM image for the octahedral-shaped NCs synthesized using no OA. HR-TEM image and FFT ED (zone axis = [111]) pattern confirm the lateral [110] direction of octahedral PbS NCs (insets). TEM images for (b) zigzagged NWs and octahedral NCs synthesized using a ratio of PbO:OA = 1:1; (c) uniformly grown zigzagged PbS NWs (avg diameter =50 nm) synthesized using a ratio of PbO:OA = 1:3 (PS1). (d) SEM image of PS1 and (e) its HRTEM images, revealing the highly crystalline lattice planes of cubic PbS (d_{200} = 3.0 Å). The SAED pattern (at the [011] zone axis) confirms that the single-crystalline NWs grew in the [100] direction (inset). (f) TEM image showing the straight NWs (avg diameter =30 nm) synthesized using a ratio of PbO:OA = 1:5; (g) HRTEM images of a representative PbS NW. The SAED pattern (zone axis = [111]) confirms the [110] growth direction (inset). (h) TEM image showing the bicrystalline PbS NWs (avg diameter = 50 nm), synthesized using a ratio of PbO:OA = 1:8; (i) HRTEM images of a twinned PbS NW. The FFT ED patterns (zone axis = [011]) confirm the [112] growth direction and [111] twinning direction (insets). The ED patterns i and iii correspond to those of the twin NW segments and pattern ii corresponds to their twin plane region, showing two NW segments share the $[111]_c/[\bar{1}\bar{1}\bar{1}]_c$ spots.

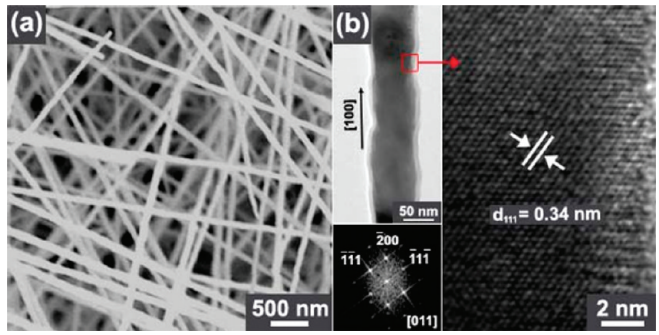

Figure 2. (a) SEM micrograph of high-density PbS NWs grown on the substrates synthesized using the CVT method (PS2). (b) TEM image of a representative PbS NW (avg diameter = 50 nm), and its corresponding TEM image. The FFT ED pattern (at the [011] zone axis) confirms that the single-crystalline PbS NW grew in the [100] direction (inset).

twin plane. It is known that the formation of the [111] twinning structure is favorable, due to its having the lowest surface and volume energies.[82] The present PbS NWs consistently show the [111] twin boundary. As the growth rate drastically decreases, defect sites would develop in the lowest surface-energy planes. The slower growth rate would produce the attachment of two seeds, resulting in the larger diameter than that grown under PbO:OA = 1:5.

CVT Synthesis of PbS NWs. High-purity PbS NWs were synthesized on Au catalytic nanoparticle-deposited Si substrates by the thermal evaporation of $PbCl_2$ and S powders using the VLS growth mechanism. The Pb and S vapors melt into the Au nanoparticles, followed by the saturation and precipitation from eutectic-melt droplets. Figure 2a shows the SEM image of the high-density PbS NWs grown on the substrates. The TEM image reveals that their diameter is in the range of 60−100 nm, with an average value of 50 nm (Figure 2b). They have an uneven surface, but no nanoparticle impurities. The HRTEM images of a selected PbS NW, revealing its perfect single-crystalline nature. The (111) fringes are separated by a distance of 3.4 Å, which is equal to that of cubic PbS crystal. The corresponding FFT ED pattern, measured at the [011] zone axis, confirms their [100] growth direction (inset). The EDX analysis confirms that the [Pb]/[S] ratio is 1 ± 0.1, as shown in the Supporting Information, Figure S1. We refer to this PbS NW sample, as "**PS2**".

The CVT growth of PbS NWs using $PbCl_2$ and S sources was demonstrated by a number of research groups.[29−34] All of these PbS NWs have the [100] growth direction, which is consistent with the present work. The growth temperature would be a major factor in controlling the growth direction of the PbS NWs, as shown in our previous work on MnSe NWs.[83] The preferential growth direction of the PbS NWs is [100] at the present growth temperature (700 °C). If the growth temperature is lowered (so it falls into "thermodynamically controlled reaction regime"), the NWs would grow through the higher surface energy [110] direction that needs the lower activation energy, as occurs in the following substitution reaction synthesis at 600 °C.

Gas-Phase Substitution Reaction from CdS NWs to PbS NWs. CdS NWs (mixed with the CdS NBs) were synthesized by the thermal evaporation of CdS powders, as described elsewhere.[48] Figure 3a shows a typical SEM image of the high-density CdS

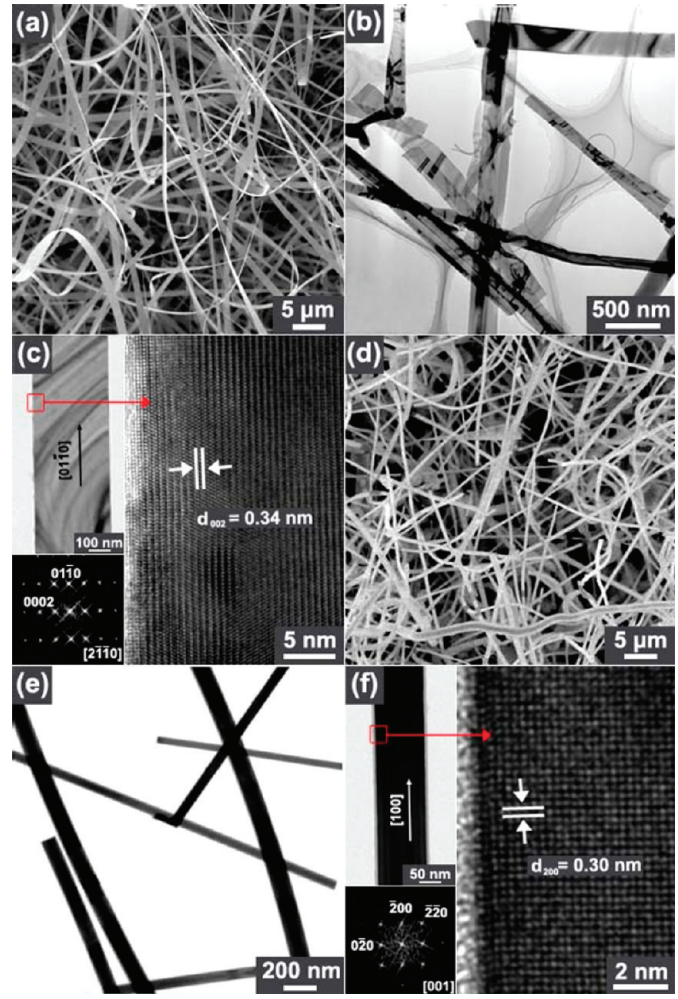

Figure 3. (a) SEM micrograph of high-density CdS NWs/NBs produced using the thermal evaporation method. (b) TEM image showing the general morphology of the CdS NWs/NBs. (c) HRTEM images and FFT ED pattern (zone axis = $[2\bar{1}\bar{1}0]$) revealing the [010] growth direction. (d) SEM micrograph of high-density PbS NWs/NBs (PS3) produced by the complete substitution of the CdS NWs/NBs at 700 °C. (e) TEM image showing the general morphology of the PbS NWs. (f) HRTEM images of a representative PbS NW and its corresponding FFT ED pattern (zone axis = [001]) confirming the [100] growth direction (inset).

NWs/NBs. The TEM image reveals that their width is in the wide range of 50−300 nm, with an average value of 100 nm (Figure 3b). The HRTEM images and FFT ED pattern (at the [$2\bar{1}\bar{1}0$] zone axis) show that the CdS NBs have a perfect single-crystalline nature with the [010] growth direction (Figure 3c). The (002) fringes are separated by a distance of about 3.4 Å, which is close to that of the bulk CdS (JCPDS card no. 41-1049; a = 4.140 Å, c = 6.719 Å). Figure 3d shows the SEM image of the high-density PbS NWs/NBs, produced by the complete gas-phase substitution reaction (60 min) of the CdS NWs/NBs using $PbCl_2$ vapor at 700 °C. Figure 3e corresponds to a TEM image showing their general morphology, in which the surface is smooth and the average diameter is 100 ± 50 nm. The HRTEM images reveal that the PbS NWs consist of highly crystalline cubic PbS having the [100] growth direction (Figure 3f). The distance between the (200) planes is about 3.0 Å. Their corresponding FFT ED pattern confirms their single-crystalline nature (inset). The EDX elemental line scanning and spectrum revealed that only Pb and S were present over the whole NWs, with no trace of Cd, as shown in the Supporting Information, Figure S1. All of the PbS NWs we observed had the same [100] growth direction. We refer to this PbS NW sample, as "**PS3**".

As the substution temperature was lowered to 600 °C and the reaction time reduced to 10 min, the CdS NWs or NBs were partially converted to the PbS ones. We refer to this sample, as "**PCS**", and examined the four types of PbCdS NWs or NBs (referred to as "**PCS1**−**PCS4**") to comprehend their substitution process. Figure 4a shows a selected NB having no Cd composition. We refer to this NB as "**PCS1**". The HRTEM images and FFT ED pattern (zone axis = [112]) reveal their single-crystalline nature and [110] growth direction. The (111) fringes are separated by a distance of about 3.4 Å, which is close to that of the bulk PbS. The EDX elemental mapping reveals the absence of Cd element over the whole NW.

For a number of NBs having a width of 200−300 nm, the substituted PbS is clearly separated from the residual CdS. Figure 4b shows the TEM images of the CdS−PbS NB heterostructures having a width of 200 nm. The PbS segment is produced at the end of the CdS NB, with a separation line perpendicular to the long axis. We refer to this sample as "**PCS2**". The EDX elemental mapping of another NB reveals the separation of PbS and CdS along the perpendicular direction of the belt axis. The HRTEM images and corresponding FFT ED pattern confirm the [110] direction of the PbS NB part at the [011] zone axis, being parallel to the belt axis. The (111) fringes of PbS are separated by a distance of about 3.4 Å, which is close to that of the bulk PbS. The belt axis of the CdS NB coincides with the [010] direction, as shown in the FFT ED pattern at the [$2\bar{1}\bar{1}0$] zone axis. The (010) and (002) fringes of the CdS NBs are separated by a distance of about 3.6 and 3.4 Å, which

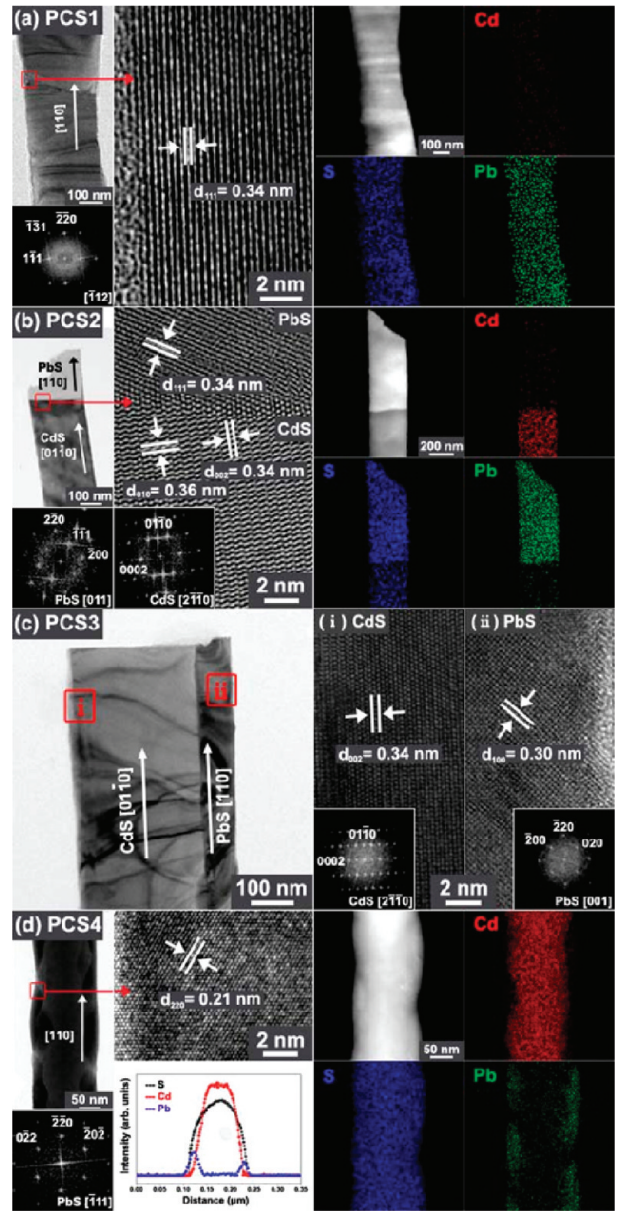

Figure 4. (a) HRTEM images for a selected PbS NB (PCS1) produced by the substitution reaction at 600 °C. The FFT ED pattern (zone axis = [112]) confirms the [110] growth direction (inset). EDX elemental mapping reveals no Cd content. (b) HRTEM image for the PbS-CdS NB heterostructure (PCS2), revealing the CdS and PbS segments separated perpendicular to the belt axis. The FFT ED pattern confirms the [110] direction of PbS (zone axis = [011]) and the [010] growth direction of CdS (zone axis = [$2\bar{1}\bar{1}$0]). EDX elemental mapping of another NB reveals the formation of PbS NB attached at the end of the CdS NB. (c) TEM image for another PbS-CdS NB heterostructure (PCS3), having the CdS and PbS segments with a separation line along the belt axis. The insets correspond to the FFT ED patterns confirming the [110] growth direction of PbS (zone axis = [001]) and the [010] growth direction of CdS (zone axis = [$2\bar{1}\bar{1}$0]). (d) TEM image for the cable structure NW (PCS4) having a CdS core and PbS shell. The FFT ED pattern (zone axis = [111]) confirms the [110] direction of the PbS shell along the wire axis (inset). The EDX line-scanning and elemental mapping reveals the PbS shell sheathing the CdS core.

is close to that of the bulk CdS. The junction between the CdS and PbS domains is rendered clearly visible by the CdS (010), CdS (002), and PbS (111) fringes. This sug-

gests that the small lattice matching (<5%) between these planes drives the substitution reaction leading the to the growth of the PbS.

Figure 4c corresponds to the HRTEM images of another CdS−PbS NB heterostructure, showing the PbS segment formed on one side of the CdS NB, with a separation line parallel to the belt axis. We refer to this NB as "**PCS3**". The corresponding FFT ED patterns confirm the [010] direction of CdS (at the $[2\bar{1}\bar{1}0]$ zone axis) and the [110] direction of PbS (at the [001] zone axis) along the belt axis. The TEM and ED pattern analysis of these two heterostructures (**PCS2** and **PCS3**) indicates that the cation substitution takes place without any preference as to the axial or perpendicular direction of the NBs.

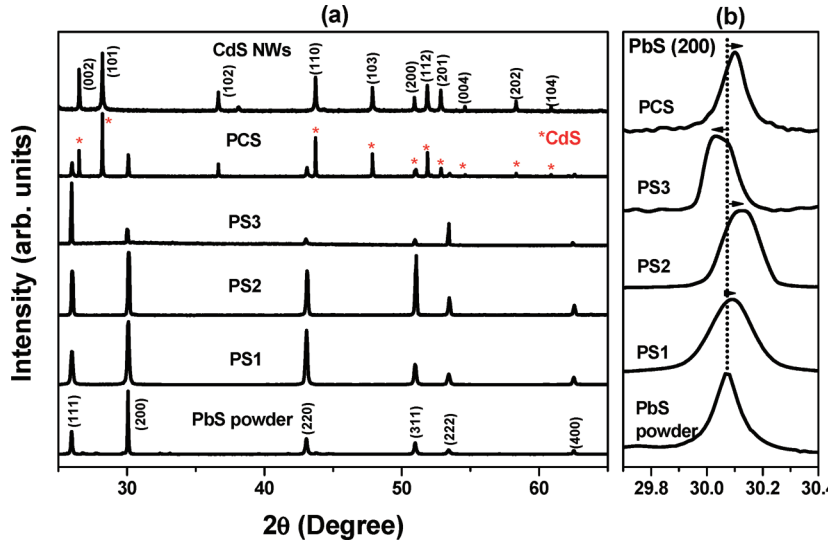

Figure 5. (a) XRD pattern of the PbS powder, PS1−PS3, PCS, CdS NW samples; (b) magnified PbS (200) peaks of the PbS powder, PS1−PS3, and PCS samples.

On the other hand, the CdS NWs with diameters less than 200 nm usually undergo the cation substitution preferentially along the axial direction. Figure 4d shows the core−shell cable structure NWs, having a higher Pb composition at the outerlayers of CdS NW core. We refer to this core−shell NW as "**PCS4**". The EDX line scanning and elemental mapping demonstrate that the PbS shell sheathed the CdS NW core. The average value of the Pb content ([Pb]/[Pb]+[Cd]) over the whole NW is estimated to be 22%. The HRTEM images and corresponding FFT ED pattern (at the [111] zone axis) of the PbS shell part confirm its [110] direction along the wire axis. The (220) fringes are separated by a distance of about 2.1 Å, which is close to that of the bulk PbS. We observed another NW, having PbS on one side along the axial direction, as shown in the Supporting Information, Figure S2.

In the gas-phase substitution reaction, the growth direction of the PbS NWs evolved from the [110] to [100] direction as the temperature increased from 600 to 700 °C. This is entirely consistent with the prediction that the higher surface-energy growth along the [110] direction is allowed at the lower temperature, 600 °C ("thermodynamically controlled growth condition"), whereas the lower surface-energy growth along the [100] direction becomes active at the higher temperature, 700 °C ("kinetically controlled growth condition"). At the higher growth temperature, the increased thermal energy allows the lower surface-energy direction growth that needs the higher activation energy barrier. The growth of the PbS NWs *via* the substitution and CVT reactions at 700 °C produced the same [100] growth direction, suggesting that the growth temperature is a major factor in determining the growth direction of the NWs when the vapor phase is involved in the growth process.

Using the solution-phase cation exchange reaction, Alivisatos group showed that wurtzite CdS nanorod (growth direction = [001]) undergone partial exchange to Cu_2S, followed by conversion of the Cu_2S portion to PbS.[47] After complete removal of Cu_2S, the nanorod consisted of the PbS grain attached epitaxially to the CdS, with $(111)_{PbS}/(002)_{CdS}$ and $(224)_{PbS}/(110)_{CdS}$. The elongated dimension of CdS transforms to the [111] direction of PbS. In contrast, the present NB contains the PbS segment attached epitaxially to the CdS, with $(110)_{PbS}/(010)_{CdS}$. The HRTEM images of the junction part between the CdS and PbS domains in the PbS−CdS heterostructures suggest that the good lattice matching between the PbS (111) and CdS (010) (or CdS (002)) planes promotes the substitution reaction leading to the growth of the PbS crystals. This partial substitution provides very important information for understanding the substitution reaction.

XRD and XPS. Figure 5a displays the high-resolution XRD patterns of the **PS1**−**PS3**, **PCS**, CdS NW, and PbS powder samples. The XRD peak of the **PS1**−**PS3** NW samples confirms that they are all highly crystalline cubic PbS crystals without any oxide phases. The **PCS** sample shows both rock-salt PbS and wurtzite CdS peaks. The PbS (200) peak is displayed on a magnified scale (Figure 5b). The **PS1**, **PS2**, and **PCS** samples show a slight shift to higher angles (<0.03 degrees) compared to that of the PbS powders. This shift to a higher angle can be attributed to the formation of an oxide layer on the surface, as discussed later using the XPS data. In contrast, the **PS3** samples (synthesized by substitution at 700 °C) exhibit a

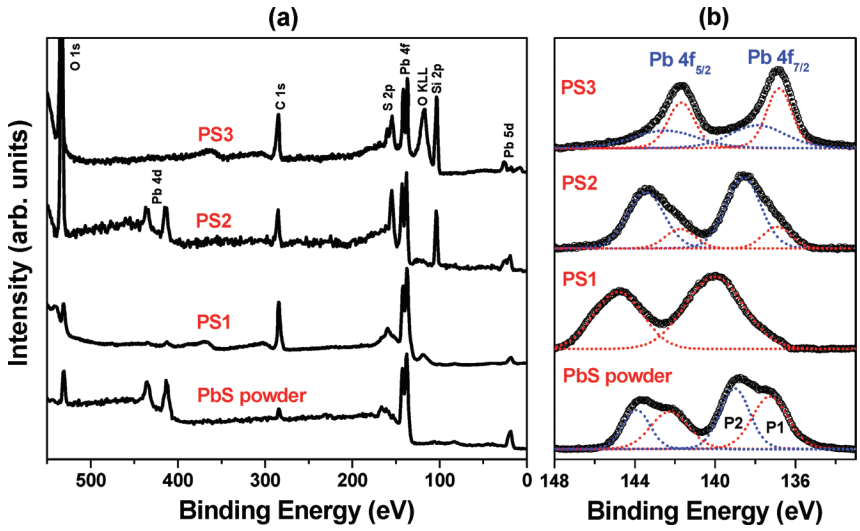

Figure 6. (a) XPS survey scan and (b) fine-scanned Pb $4f_{7/2}$ and $4f_{5/2}$ peaks of PbS powder and PS1−PS3 samples. The data points (open circles) of each peak are fitted by two Voigt functions, P1 (red-colored dotted lines) and P2 (blue-colored dotted lines).

shift to a lower angle (0.05 degrees), indicating the lesser incorporation of oxygen atoms.

In the case of the **PCS** sample, the peak position shifts negligibly relative to that of the pure PbS NW samples (**PS1** and **PS2**). If the Cd^{2+} ions ($r(Cd^{2+}) = 0.92$ Å) were to reside at the sites of the larger radius Pb^{2+} ions ($r(Pb^{2+}) = 1.12$ Å), they would reduce the lattice constant of PbS, which is inconsistent with the present result. The absence of any peak broadening also implies the absence of any defects in the PbS structure after the substitution. The magnified-scaled CdS peaks also show no peak shift or broadening relative to those of the CdS NWs (not shown here), suggesting that the growth of PbS does not deteriorate the crystallinity of CdS. Therefore, the majority of the PbS NWs (or NBs) can grow by forming a PbS domain separated from the CdS NWs, during the substitution reaction.

Figure 6 displays the XPS survey scan of the PbS powder and **PS1**−**PS3** samples, showing only Cd and S peaks. The fine-scanned Pb $4f_{7/2}$ and $4f_{5/2}$ peaks of the **PS1**−**PS3** samples were compared with those of PbS powder, as shown in Figure 6b. Each peak was resolved into two bands, P1 and P2, by fitting it into the Voigt function. For the Pb $4f_{7/2}$ peak, the P1 band at 137.3 eV and the P2 band at 139.0 eV are assigned to the Pb−S and Pb−O bonding structures, respectively. The **PS2** sample shows a significant Pb−O band, while that of the PS3 sample has a much lower intensity. The binding energy of the PS1 sample is shifted to the higher energy region and is distributed over a broader range, so the peak cannot be resolved into two bands. This could be due to the presence of residual ligands on the NW surface. The XPS result consistently indicates that the **PS3** samples have high quality PbS NWs with a thinner oxide-layer, which are suitable for electronic devices.

PbS NW FETs. We fabricated the PbS NW FET electrodes by the following procedure. The nanowires, dispersed in isopropyl alcohol (IPA), were dropped onto a Si substrate with a 300-nm-thick thermally grown SiO_2 layer on which alignment marks had been made. The spatial position and orientation of the nanowires were recorded by digitizing the coordinates from the optical microscopy images. The electrical leads were defined on the selected NW using electron beam lithography. A plasma etching system was used to remove the oxide layer from the outer surface of the NW. For the Ohmic contact, Cr (20 nm)/Au (80 nm) films were deposited on the contact area by electron beam evaporation. The etching and deposition of the electrodes were carried out *in situ* without breaking the vacuum, in order to prevent the further formation of the oxide layer. The underlying Si substrate was used as the back gate by forming an Ohmic contact with an Al electrode.

We selected a PbS NW from the PS3 sample, because of the thinner oxide-layer on its surface. Figure 7a shows the reproducible source−drain current (I) *versus* voltage (V_{SD}) curves at 10 different gate voltages ($V_G = -20$ to 0 V by 2 V step) obtained from the PbS NW FET device. The SEM image of the NW

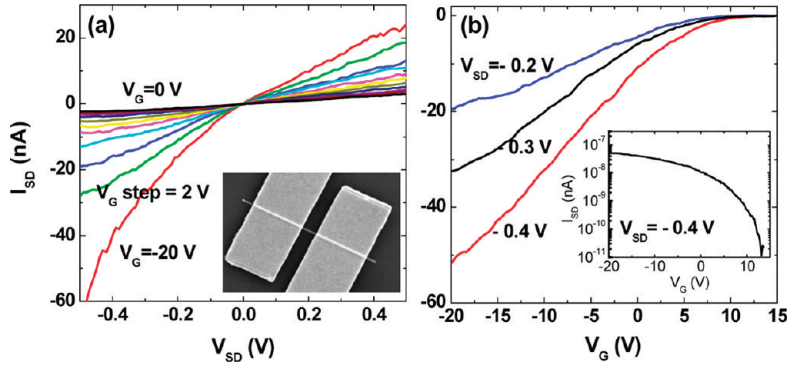

Figure 7. Current *versus* source-drain ($I-V_{SD}$) curves at different gate voltages (V_G = 0 to −20 V with 2 V step) of an FET made of a single PbS NW (PS3). The inset corresponds to the SEM image of the PbS NW FET. (b) $I-V_G$ data at $V_{SD} = -0.2$, −0.3, and −0.4 V. The inset represents the log-scaled plot for $V_{SD} = -0.4$ V.

FET is shown in the inset. The channel length is 1 μm and the diameter is 150 nm. The two-terminal $I-V_{SD}$ curves exhibit a nearly linear response at zero bias and, thus, the contacts behave, in practical terms, as Ohmic ones. For a given V_{SD}, I increases considerably with increasing negative V_G, indicating the *p*-type semiconductor characteristics of the PbS NW, with a moderate carrier concentration.

To determine the efficiency of the gating behavior, transconductance measurements (I *vs* V_G) were obtained using $V_{SD} = -0.2$, -0.3, and -0.4 V (Figure 7b). At more positive V_G values, there is no measurable current through the wire. As the negative V_G increases, the current linearly increases with respect to V_G. The threshold voltage for current onset (V_{th}) is 12.5 V, as shown in the logarithmic plot of $V_{SD} = -0.4$ V (inset). Note that this V_{th} value is the average of all three V_{SD} values. The on−off current ratio (I_{ON}/I_{OFF}) of $\sim 10^4$ is deduced. From the linear region of the $I-V_G$ curve at a fixed $V_{SD} = -0.4$ V, the transconductance ($g_m = dI/dV_G$) can be extrapolated. The maximum channel mobility of the device, μ_h, was estimated to be 10 $cm^2\ V^{-1}\ s^{-1}$, using the equation, $\mu_h = g_m(L^2/(CV_{SD}))$, where L is the channel length (=1 μm) of the NW FET and C is the capacitance of the nanowire.[84] The capacitance of the nanowire, C, is given by $C = 2\pi\varepsilon\varepsilon_0 L/\ln(2h/r)$, where ε is the relative dielectric constant of SiO_2 (=3.9), h is the thickness of the silicon oxide layer (=300 nm), and r is the radius of the nanowire (75 nm). The mobility of the present NW is higher than that of the PbS bulk, 5 $cm^2\ V^{-1}\ s^{-1}$ at $n = 2.5 \times 10^{17}\ cm^{-3}$.[85] It is also higher than that (2.7 $cm^2\ V^{-1}\ s^{-1}$) of the *p*-type PbSe NW ($n = 6 \times 10^{18}\ cm^3$) measured by Yang and co-workers.[86] Compared to the **PS3** NWs, the current level of the other samples (**PS1** and **PS2**) is lower by a factor of at least 10, probably due to their oxide layered surface (Supporting Information, Figure S3). The PbS NW selected from these samples shows *p*-type semiconductor characteristics, like that of the PS3 sample.

CONCLUSIONS

We synthesized single-crystalline PbS NWs using three different routes: (i) the solvothermal (**PS1**), (ii) CVT (**PS2**), and (iii) gas-phase cation substitution reaction of pregrown CdS NWs (**PS3**). The PbS NWs consisted of single-crystalline rock-salt structure PbS uniformly grown in the controlled growth direction. The solvothermal reaction produced the [100], [110], and [112] growth directions in a controlled manner. As the OA concentration increases, the growth occurs more slowly under the thermodynamically controlled conditions, inducing the evolution of the growth direction toward the higher surface-energy directions, that is, [100] → [110] → [112].

The CVT method (at 700 °C) produced single-crystalline PbS NWs grown along the [100] direction. The complete substitution reaction of the CdS NWs (at 700 °C) produced single-crystalline PbS NWs preferentially grown along the [100] direction. At a lower temperature in the substitution reaction (600 °C), PbS NWs were produced with the [110] growth direction. The higher surface-energy growth along the [110] direction is allowed in the thermodynamically controlled lower temperature regime, whereas the lower surface-energy growth along the [100] direction becomes active in the kinetically controlled higher temperature regime. We also observed that the conversion from single-crystalline CdS NWs into PbS NWs proceeds through CdS−PbS heterostructures as an intermediate. The conversion to the PbS NWs would be expected to take place through the lattice matched PbS (111) and CdS (010)/(002) planes.

The synchrotron-radiation XRD and XPS analysis indicates that the PS3 sample consists of PbS NWs with a thinner oxide layer. The NW FET devices fabricated using an individual PbS NW showed *p*-type semiconductor characteristics, irrespective of the synthesis method. For the PbS NWs of the PS3 sample, the highest value of the mobility was determined to be about 10 $cm^2\ V^{-1}\ s^{-1}$.

EXPERIMENTAL SECTION

For the solvothermal synthesis, lead oxide (PbO, 99.999%), sulfur (S) powder (99.99%), trioctylphosphine (TOP, 90%), oleic acid (OLA, $C_8H_{17}{=}C_8H_{15}{-}COOH$, 90%), octylamine (OA, $C_8H_{17}{-}NH_2$), and 1-octadecene (ODE, $C_{17}H_{34}{=}CH_2$, tech grade, 90%) were purchased from Sigma-Aldrich or Alfa Co. The procedure was divided into three steps: (1) 178.6 mg (0.8 mmol) of PbO and 0.64 mL (2 mmol) of OLA were dissolved in 3.2 mL (10 mmol) of ODE in a 50 mL three-neck flask equipped with a condenser, and the mixture was heated to 300 °C under argon flow; (2) a solution of 3.85 mg (1.2 mmol) of S dissolved in 1.8 mL (4 mmol) of TOP was swiftly injected into the heated solution, and the reaction mixture was then cooled to 270 °C; (3) the mixture was maintained at 270 °C for 10 min to allow for the growth of the PbS NCs. For the addition of OA, 0.8−8 mmol dissolved in the S-TOP solution was injected into the hot solution in step 2. The other reaction conditions were kept the same as those described above. The molar ratio of the precursors and ligands is PbO:S:OLA:TOP:OA = 1:1.5:2.5:5:0−10.

For the CVT synthesis of the PbS NWs, lead(II) chloride ($PbCl_2$, 99.999%, Aldrich) and S (99.8%, Aldrich) powders were placed inside a quartz tube reactor. A silicon substrate on which Au nanoparticles were deposited was positioned at a distance of 10 cm from the PbS source. As the source was allowed to evaporate at 800 °C for 2 h under an argon flow (300 sccm), the NWs grew on the substrate at 700 °C. To obtain the chemical conversion of the CdS NWs into the PbS NWs, we synthesized the CdS NWs as a first step. CdS (99.98%, Aldrich) powder was placed a few cm apart from an Au nanoparticles-deposited Si substrate inside a quartz tube reactor. As the source was evaporated at 850 °C for 1 h under argon flow, high-density CdS NWs were deposited on the substrates at about 700 °C.[37a] Then the pregrown CdS NWs were placed in the reactor and $PbCl_2$ powders were evaporated for 10−60 min at temperatures in the range of 600−700 °C.

The products were analyzed by scanning electron microscopy (SEM, Hitachi S-4700), field-emission transmission electron microscopy (TEM, FEI TECNAI G^2 200 kV and Jeol JEM 2100F),

high-voltage TEM (HVEM, Jeol JEM ARM 1300S, 1.25 MV), electron diffraction (ED), and energy-dispersive X-ray fluorescence spectroscopy (EDX). High-resolution X-ray diffraction (XRD) patterns were obtained using the 8C2 and 3C2 beamlines of the Pohang Light Source (PLS) with monochromatic radiation (λ = 1.54520 Å). X-ray photoelectron spectroscopy (XPS) was carried out using the 8A1 beamline of the Pohang Light Source (PLS) and a laboratory-based spectrometer (VG Scientifics ESCALAB 250) using a photon energy of 1486.6 eV (Al Kα).

Acknowledgment. This study was supported by the NRF (Grants R01-2008-000-10825-0; 2008-02364; 2008-314-C00175; 2009-0082528) and MKE under the auspices of the ITRC support program supervised by the IITA (2008-C1090-0804-0013). This research was also supported by the WCU (World Class University) program through the NRF funded by the Ministry of Education, Science and Technology (R31-10035). The HVEM (Daejeon), XRD (Taegu), and XPS (Pusan) measurements were performed at the KBSI. The experiments at the PLS were partially supported by MOST and POSTECH.

Supporting Information Available: EDX data, TEM images, and *I*−*V* curve of PbS NW FET. This material is available free of charge *via* the Internet at http://pubs.acs.org.

REFERENCES AND NOTES

1. Hu, J.; Odom, T. W.; Lieber, C. M. Chemistry and Physics in One Dimension: Synthesis and Properties of Nanowires and Nanotubes. *Acc. Chem. Res.* **1999**, *32*, 435–445.
2. Xia, Y. N.; Yang, P. D.; Sun, Y. G.; Wu, Y. Y.; Mayers, B.; Gates, B.; Yin, Y. D.; Kim, F.; Yan, H. Q. One-Dimensional Nanostructures: Synthesis, Characterization, and Applications. *Adv. Mater.* **2003**, *15*, 353–389.
3. Huang, Y.; Duan, X.; Cui, Y.; Lauhon, L. J; Kim, K. -H.; Lieber, C. M. Logic Gates and Computation from Assembled Nanowire Building Blocks. *Science* **2001**, *294*, 1313–1317.
4. Gudiksen, M. S.; Lauhon, L. J.; Wang, J.; Smith, D. C.; Lieber, C. M. Growth of Nanowire Superlattice Structures for Nanoscale Photonics and Electronics. *Nature (London)* **2002**, *415*, 617–620.
5. Patolsky, F.; Zheng, G.; Hayden, O.; Lakadamyali, M.; Zhuang, X.; Lieber, C. M. Electrical Detection of Single Viruses. *Proc. Natl. Acad. Sci. U.S.A.* **2004**, *101*, 14017–14022.
6. Wise, F. W. Lead Salt Quantum Dots: The Limit of Strong Quantum Confinement. *Acc. Chem. Res.* **2000**, *33*, 773–780.
7. Bakueva, L.; Musikhin, S.; Hines, M. A.; Chang, T. -W. F.; Tzolov, M.; Scholes, G. D.; Sargent, E. H. Size-Tunable Infrared (1000−1600 nm) Electroluminescence from PbS Quantum-Dot Nanocrystals in a Semiconducting Polymer. *Appl. Phys. Lett.* **2003**, *82*, 2895–2897.
8. Bakueva, L.; Gorelikov, I.; Musikhin, S.; Zhao, X. S.; Sargent, E. H.; Kumacheva, E. PbS Quantum Dots with Stable Efficient Luminescence in the Near-IR Spectral Range. *Adv. Mater.* **2004**, *16*, 926–929.
9. McDonald, S. A.; Konstantatos, G.; Zhang, S. G.; Cyr, P. W.; Klem, E. J. D.; Levina, L.; Sargent, E. H. Solution-Processed PbS Quantum Dot Infrared Photodetectors and Photovoltaics. *Nat. Mater.* **2005**, *4*, 138–142.
10. Nozik, A. J. Exciton Multiplication and Relaxation Dynamics in Quantum Dots: Applications to Ultrahigh-Efficiency Solar Photon Conversion. *Inorg. Chem.* **2005**, *44*, 6893–6899.
11. Rauch, T.; Böberl, M; Tedde, S. F.; Fürst, J.; Kovalenko, M. V.; Hesser, G.; Lemmer, U.; Heiss, W.; Hayden, O. Near-Infrared Imaging with Quantum-Dot-Sensitized Organic Photodiodes. *Nat. Photonics* **2009**, *3*, 332–336.
12. Gao, F.; Lu, Q.; Liu, X.; Yan, Y.; Zhao, D. Controlled Synthesis of Semiconductor PbS Nanocrystals and Nanowires Inside Mesoporous Silica SBA-15 Phase. *Nano Lett.* **2001**, *1*, 743–748.
13. Mukherjee, P. K.; Chatterjee, K.; Chakravorty, D. Semiconductor to Metal Transition in PbS Nanowires Grown in Mica Channels. *Phys. Rev. B* **2006**, *73*, 035414.
14. Wu, C.; Shi, J. -B.; Chen, C. -J.; Chen, Y. -C.; Wu, P. -F.; Lin, J. -Y. Correlation between Structural and Optical Properties of 30 and 60 nm Lead Sulfide Nanowires. *Mater. Lett.* **2007**, *61*, 4659–4661.
15. Yu, D.; Wang, D.; Meng, Z.; Lu, J.; Qian, Y. Synthesis of Closed PbS Nanowires with Regular Geometric Morphologies. *J. Mater. Chem.* **2002**, *12*, 403–405.
16. Tang, K.; Qian, Y.; Zeng, J.; Yang, X. Solvothermal Route to Semiconductor Nanowires. *Adv. Mater.* **2003**, *15*, 448–450.
17. Kuang, D.; Xu, A.; Fang, Y.; Liu, H.; Frommen, C.; Fenske, D. Surfactant-Assisted Growth of Novel PbS Dendritic Nanostructures *via* Facile Hydrothermal Process. *Adv. Mater.* **2003**, *15*, 1747–1750.
18. Chen, J.; Chen, L.; Wu, L. -M. The Solventless Syntheses of Unique PbS Nanowires of X-Shaped Cross Sections and the Cooperative Effects of Ethylenediamine and a Second Salt. *Inorg. Chem.* **2007**, *46*, 8038–8043.
19. Saraidarov, T.; Reisfeld, R.; Sashchiuk, A.; Lifshitz, E. Synthesis and Characterization of PbS Nanorods and Nanowires. *Phys. E.* **2007**, *37*, 173–177.
20. Ding, B.; Shi, M.; Chen, F.; Zhou, R.; Deng, M.; Wang, M.; Chen, H. Shape-Controlled Syntheses of PbS Submicro-/Nano-Crystals *via* Hydrothermal Method. *J. Cryst. Growth* **2009**, *311*, 1533–1538.
21. Wang, S. H.; Yang, S. H. Preparation and Characterization of Oriented PbS Crystalline Nanorods in Polymer Films. *Langmuir* **2000**, *16*, 389–397.
22. Yong, K. -T.; Sahoo, Y.; Choudhury, K. R.; Swihart, M. T.; Minter, J. R.; Prasad, P. N. Control of the Morphology and Size of PbS Nanowires Using Gold Nanoparticles. *Chem. Mater.* **2006**, *18*, 5965–5972.
23. Patla, I.; Acharya, S.; Zeiri, L.; Israelachvili, J.; Efrima, S.; Golan, Y. Synthesis, Two-Dimensional Assembly, and Surface Pressure-Induced Coalescence of Ultranarrow PbS Nanowires. *Nano Lett.* **2007**, *7*, 1459–1462.
24. Acharya, S.; Gautam, U. K.; Sasaki, T.; Bando, Y.; Golan, Y.; Ariga, K. Ultra Narrow PbS Nanorods with Intense Fluorescence. *J. Am. Chem. Soc.* **2008**, *130*, 4594–4595.
25. Wang, Z.; Zhao, B.; Zhang, F.; Mao, W.; Qian, G.; Fan, X. Novel Single-Crystal PbS Nanowires Directed by [200]. *Mater. Lett.* **2007**, *61*, 3733–3735.
26. Talapin, D. V.; Yu, H.; Shevchenko, E. V.; Lobo, A.; Murray, C. B. Synthesis of Colloidal PbSe/PbS Core−Shell Nanowires and PbS/Au Nanowire−Nanocrystal Heterostructures. *J. Phys. Chem. C* **2007**, *111*, 14049–14054.
27. Mokari, T.; Habas, S. E.; Zhang, M.; Yang, P. Synthesis of Lead Chalcogenide Alloy and Core−Shell Nanowires. *Angew. Chem., Int. Ed.* **2008**, *47*, 5605–5608.
28. Warner, J. H.; Cao, H. Shape Control of PbS Nanocrystals Using Multiple Surfactants. *Nanotechnology* **2008**, *19*, 305605.
29. Ge, J. -P.; Wang, J.; Zhang, H. -X.; Wang, X.; Peng, Q.; Li, Y. -D. Orthogonal PbS Nanowire Arrays and Networks and Their Raman Scattering Behavior. *Chem.—Eur. J.* **2005**, *11*, 1889–1894.
30. Afzaal, M.; O'Brien, P. Silica Coated PbS Nanowires. *J. Mater. Chem.* **2006**, *16*, 1113–1115.
31. Fardy, M.; Hochbaum, A. I.; Goldberger, J.; Zhang, M. M.; Yang, P. Synthesis and Thermoelectrical Characterization of Lead Chalcogenide Nanowires. *Adv. Mater.* **2007**, *19*, 3047–3051.
32. Bierman, M. J.; Albert Lau, Y. K.; Jin, S. Hyperbranched PbS and PbSe Nanowires and the Effect of Hydrogen Gas on Their Synthesis. *Nano Lett.* **2007**, *7*, 2907–2912.
33. Bierman, M. J.; Albert Lau, Y. K.; Kvit, A.; Schmitt, A. L.; Jin, S. Dislocation-Driven Nanowire Growth and Eshelby Twist. *Science* **2008**, *320*, 1060–1063.
34. Albert Lau, Y. K.; Chernak, D. J.; Bierman, M. J.; Jin, S. Epitaxial Growth of Hierarchical PbS Nanowires. *J. Mater. Chem.* **2009**, *19*, 934–940.
35. Shen, X. -F.; Yan, X. -P. Environmentally Benign and Cost-Effective Synthesis of Well-Aligned Nanoporous PbS Nanowire Architectures. *J. Mater. Chem.* **2008**, *18*, 4631–4635.

36. Warner, J. H. Self-Assembly of Ligand-Free PbS Nanocrystals into Nanorods and Their Nanosculpturing by Electron-Beam Irradiation. *Adv. Mater.* **2008**, *20*, 784–787.
37. Song, J. H.; Messer, B.; Wu, Y.; Kind, H.; Yang, P. MMo_3Se_3 ($M = Li^+$, Na^+, Rb^+, Cs^+, NMe_4^+) Nanowire Formation *via* Cation Exchange in Organic Solution. *J. Am. Chem. Soc.* **2001**, *123*, 9714–9715.
38. Dloczik, L.; Engelhardt, R.; Ernst, K.; Fiechter, S.; Sieber, I.; Könenkamp, R. Hexagonal Nanotubes of ZnS by Chemical Conversion of Monocrystalline ZnO Columns. *Appl. Phys. Lett.* **2001**, *78*, 3687–3689.
39. Dloczik, L.; Engelhardt, R.; Ernst, K.; Lux-Steiner, M. C.; Könenkamp, R. Zinc Sulfide Columns by Chemical Conversion of Zinc Oxide. *Sens. Actuators, B* **2002**, *84*, 33–36.
40. Dloczik, L.; Könenkamp, R. Nanostructure Transfer in Semiconductors by Ion Exchange. *Nano Lett.* **2003**, *3*, 651–653.
41. Dloczik, L.; Lux-Steiner, M. C.; Könenkamp, R. Study on the Preparation of Structured $CuInS_2$ Films by Ion Exchange Processes. *Thin Solid Films* **2003**, *431*, 131–134.
42. Jeong, U.; Xia, Y.; Yin, Y. Large-Scale Synthesis of Single-Crystal CdSe Nanowires through a Cation-Exchange Route. *Chem. Phys. Lett.* **2005**, *416*, 246–250.
43. Jeong, U.; Camargo, P. H. C.; Lee, Y. H.; Xia, Y. Chemical Transformation: A Powerful Route to Metal Chalcogenide Nanowires. *J. Mater. Chem.* **2006**, *16*, 3893–3897.
44. Wang, R. H.; Chen, Q.; Wang, B. L.; Zhang, S.; Peng, L.-M. Strain-Induced Formation of $K_2Ti_6O_{13}$ Nanowires *via* Ion Exchange. *Appl. Phys. Lett.* **2005**, *86*, 133101.
45. Robinson, R. D.; Sadtler, B.; Demchenko, D. O.; Erdonmez, C. K.; Wang, L.-W.; Alivisatos, A. P. Spontaneous Superlattice Formation in Nanorods Through Partial Cation Exchange. *Science* **2007**, *317*, 355–358.
46. Sadtler, B.; Demchenko, D. O.; Zheng, H.; Hughes, S. M.; Merkle, M. G.; Dahmen, U.; Wang, L.-W.; Alivisatos, A. P. Selective Facet Reactivity during Cation Exchange in Cadmium Sulfide Nanorods. *J. Am. Chem. Soc.* **2009**, *131*, 5285–5293.
47. Luther, J. M.; Zheng, H.; Sadtler, B.; Alivisatos, A. P. Synthesis of PbS Nanorods and Other Ionic Nanocrystals of Complex Morphology by Sequential Cation Exchange Reactions. *J. Am. Chem. Soc.* **2009**, *131*, 16851–16857.
48. Lee, J. Y.; Kim, D. S.; Park, J. Chemical Conversion Reaction between CdS Nanobelts and ZnS Nanobelts by Vapor Transport. *Chem. Mater.* **2007**, *19*, 4663–4669.
49. Park, W. I.; Kim, H. S.; Jang, S. Y.; Park, J.; Bas, S. Y.; Jung, M.; Lee, H.; Kim, J. Transformation of ZnTe Nanowires to CdTe Nanowires Through the Formation of ZnCdTe−CdTe Core−Shell Structure by Vapor Transport. *J. Mater. Chem.* **2008**, *18*, 875–880.
50. Chou, N. H.; Schaak, R. E. Shape-Controlled Conversion of β-Sn Nanocrystals into Intermetallic M-Sn (M = Fe, Co, Ni, Pd) Nanocrystals. *J. Am. Chem. Soc.* **2007**, *129*, 7339–7345.
51. Anderson, M. E.; Buck, M. R.; Sines, I. T.; Oyler, K. D.; Schaak, R. E. On-Wire Conversion Chemistry: Engineering Solid-State Complexity into Striped Metal Nanowires Using Solution Chemistry Reactions. *J. Am. Chem. Soc.* **2008**, *130*, 14042–14043.
52. Raidongia, K.; Rao, C. N. R. Study of the Transformations of Elemental Nanowires to Nanotubes of Metal Oxides and Chalcogenides through the Kirkendall Effect. *J. Phys. Chem. C* **2008**, *112*, 13366–13371.
53. Schoen, D. T.; Peng, H.; Cui, Y. Anisotropy of Chemical Transformation from In_2Se_3 to $CuInSe_2$ Nanowires through Solid State Reaction. *J. Am. Chem. Soc.* **2009**, *131*, 7973–3975.
54. Bao, N.; Shen, L.; Gupta, A.; Tatarenko, A.; Srinivasan, G.; Yanagisawa, K. Size-Controlled One-Dimensional Monocrystalline $BaTiO_3$ Nanostructures. *Appl. Phys. Lett.* **2009**, *94*, 253109.
55. Huang, T.; Qi, L. Controlled Synthesis of PbSe Nanotubes by Solvothermal Transformation from Selenium Nanotubes. *Nanotechnology* **2009**, *20*, 025606.
56. Zhang, B.; Jung, Y.; Chung, H. -S.; Van Vugt, L.; Agarwal, R. Nanowire Transformation by Size-Dependent Cation Exchange Reactions. *Nano Lett* **2010**, *10*, 149–155.
57. Panda, A. B.; Acharya, S.; Efrima, S. Ultranarrow ZnSe Nanorods and Nanowires: Structure, Spectroscopy, and One-Dimensional Properties. *Adv. Mater.* **2005**, *17*, 2471–2474.
58. Panda, A. B.; Glaspell, G.; El-Shall, M. S. Microwave Synthesis of Highly Aligned Ultranarrow Semiconductor Rods and Wires. *J. Am. Chem. Soc.* **2006**, *128*, 2790–2791.
59. Acharya, S.; Patla, I.; Kost, J.; Efrima, S.; Golan, Y. Switchable Assembly of Utranarrow CdS Nanowires and Nanorods. *J. Am. Chem. Soc.* **2006**, *128*, 9294–9295.
60. Patla, I.; Acharya, S.; Zeiri, L.; Kost, J.; Israelachvili, J.; Efrima, S.; Golan, Y. Synthesis, Two-Dimensional Assembly, and Surface Pressure-Induced Coalescence of Ultranarrow PbS Nanowires. *Nano Lett.* **2007**, *7*, 1459–1462.
61. Min, Y.; Akbulut, M.; Belman, N.; Golan, Y.; Zasadzinski, J.; Israelachvili, J. Normal and Shear Forces Generated during the Ordering (Directed Assembly) of Confined Straight and Curved Nanowires. *Nano Lett.* **2008**, *8*, 246–252.
62. Wang, F.; Dong, A.; Sun, J.; Tang, R.; Yu, H.; Buhro, W. E. Solution−Liquid−Solid Growth of Semiconductor Nanowires. *Inorg. Chem.* **2006**, *45*, 7511–7521.
63. Wang, F.; Yu, H.; Li, J.; Hang, Q.; Zemlyanov, D.; Gibbons, P. C.; Wang, L.-W.; Janes, D. B.; Buhro, W. E. Spectroscopic Properties of Colloidal Indium Phosphide Quantum Wires. *J. Am. Chem. Soc.* **2007**, *129*, 14327–14335.
64. Pradhan, N.; Xu, H.; Peng, X. Colloidal CdSe Quantum Wires by Oriented Attachment. *Nano Lett.* **2006**, *6*, 720–724.
65. Yuhas, B. D.; Zitoun, D. O.; Pauzauskie, P. J.; He, R.; Yang, P. Transition-Metal Doped Zinc Oxide Nanowires. *Angew. Chem., Int. Ed.* **2006**, *45*, 420–423.
66. Huo, Z.; Tsung, C.; Huang, W.; Zhang, X.; Yang, P. Sub-Two Nanometer Single Crystal Au Nanowires. *Nano Lett.* **2008**, *8*, 2041–2044.
67. Fanfair, D. D.; Korgel, B. A. Twin-Related Branching of Solution-Grown ZnSe Nanowires. *Chem. Mater.* **2007**, *19*, 4943–4948.
68. Fanfair, D. D.; Korgel, B. A. ZnE (E = S, Se, Te) Nanowires Grown by the Solution−Liquid−Solid Mechanism: Importance of Reactant Decomposition Kinetics and the Solvent. *Cryst. Growth Des.* **2008**, *8*, 3246–3252.
69. Chockla, A. M.; Korgel, B. A. Seeded Germanium Nanowire Synthesis in Solution. *J. Mater. Chem.* **2009**, *19*, 996–1001.
70. Yong, K. -T.; Sahoo, Y.; Zeng, H.; Swihart, M. T.; Minter, J. R.; Prasad, P. N. Formation of ZnTe Nanowires by Oriented Attachment. *Chem. Mater.* **2007**, *19*, 4108–4110.
71. Lee, S. H.; Kim, Y. J.; Park, J. Shape Evolution of ZnTe Nanocrystals: Nanoflowers, Nanodots, and Nanorods. *Chem. Mater.* **2007**, *19*, 4670–4675.
72. Ge, M.; Liu, J. F.; Wu, H.; Yao, C.; Zeng, Y.; Fu, Z. D.; Zhang, S. L.; Jiang, J. Z. Synthesis of Germanium Nanowires. *J. Phys. Chem. C* **2007**, *111*, 11157–11160.
73. Ramirez, E.; Eradès, L.; Philippot, K.; Lecante, P.; Chaudret, B. Shape Control of Platinum Nanoparticles. *Adv. Funct. Mater.* **2007**, *17*, 2219–2228.
74. Wang, C.; Hu, Y.; Lieber, C. M.; Sun, S. Ultrathin Au Nanowires and Their Transport Properties. *J. Am. Chem. Soc.* **2008**, *130*, 8902–8903.
75. Xu, Z.; Shen, C.; Hou, Y.; Gao, H.; Sun, S. Oleylamine as Both Reducing Agent and Stabilizer in a Facile Synthesis of Magnetite Nanoparticles. *Chem. Mater.* **2009**, *21*, 1778–1780.
76. Lu, X.; Yavuz, M. S.; Tuan, H. -Y.; A; Korgel, B. A.; Xia, Y. Ultrathin Gold Nanowires Can Be Obtained by Reducing Polymeric Strands of Oleylamine−AuCl Complexes Formed *via* Aurophilic Interaction. *J. Am. Chem. Soc.* **2008**, *130*, 8900–8901.
77. Pazos-Pérez, N.; Baranov, D.; Irsen, S.; Hilgendorff, M.; Liz-Marzán, L. M.; Giersig, M. Synthesis of Flexible, Ultrathin Gold Nanowires in Organic Media. *Langmuir* **2008**, *24*, 9855–9860.
78. Cademartiri, L.; Scotognella, F.; O'Brien, P. G.; Lotsch, B. V.;

Thomson, J.; Petrov, S.; Kherani, N. P.; Ozin, G. A. Cross-Linking Bi_2S_3 Ultrathin Nanowires: A Platform for Nanostructure Formation and Biomolecule Detection. *Nano Lett.* **2009**, *9*, 1482–1486.
79. Ciuculescu, D.; Dumestre, F.; Comesana-Hermo, M.; Chaudret, B.; Spasova, M.; Farle, M.; Amiens, C. Single-Crystalline Co Nanowires: Synthesis, Thermal Stability, and Carbon Coating. *Chem. Mater.* **2009**, *21*, 3987–3995.
80. Cho, K. -S.; Talapin, D. V.; Gaschler, W.; Murray, C. B. Designing PbSe Nanowires and Nanorings through Oriented Attachment of Nanoparticles. *J. Am. Chem. Soc.* **2005**, *127*, 7140–7147.
81. Talapin, D. V.; Shevchenko, E. V.; Murray, C. B.; Titov, A. V.; Král, P. Dipole−Dipole Interactions in Nanoparticle Superlattices. *Nano Lett.* **2007**, *7*, 1213–1219.
82. Wang, Z. L. Transmission Electron Microscopy of Shape-Controlled Nanocrystals and Their Assemblies. *J. Phys. Chem. B* **2000**, *104*, 1153–1175.
83. Chun, H. J.; Lee, J. Y.; Kim, D. S.; Yoon, S. W.; Kang, J. H.; Park, J. Morphology-Tuned Growth of α-MnSe One-Dimensional Nanostructures. *J. Phys. Chem. C* **2007**, *111*, 519–525.
84. Goldberger, J.; Sirbuly, D. J.; Law, M.; Yang, P. ZnO Nanowire Transistors. *J. Phys. Chem. B* **2005**, *109*, 9–14.
85. Salim, S. M.; Hamid, O. Growth and Characterization of Lead Sulfide Films Deposited on Glass Substrates. *Ren. Energy* **2001**, *24*, 575–580.
86. Liang, W.; Hochbaum, A. I.; Fardy, M.; Rabin, O.; Zhang, M.; Yang, P. Field-Effect Modulation of Seebeck Coefficient in Single PbSe Nanowires. *Nano Lett.* **2009**, *9*, 1689–1693.